Microwave tunability in tin substituted barium titanate

Hangfeng Zhang [a,c], Henry Giddens [a], Theo Graves Saunders [a], Matteo Palma [b], Isaac Abrahams [b,*], Haixue Yan [c,*], Yang Hao [a,*]

[a] School of Electronic Engineering and Computer Science, Queen Mary University of London, Mile End Road, London E1 4NS, UK
[b] Department of Chemistry, Queen Mary University of London, Mile End Road, London E1 4NS, UK
[c] School of Engineering and Materials Science, Queen Mary University of London, Mile End Road, London E1 4NS, UK

ABSTRACT

The relationship between low and high frequency tunabilities in tin substituted barium titanate ($BaTi_{1-x}Sn_xO_3$, Sn-BTO*x*, *x* = 0.12, 0.14 and 0.16) ceramics is investigated. Although X-ray powder diffraction reveals an average non-polar cubic structure, Raman spectroscopy and piezoresponse force microscopy, along with ferroelectric and strain measurements under applied voltage reveal the presence of polar nanoclusters, while larger ferroelectric domains are seen in Sn-BTO12. Although the highest low frequency tunability was obtained for Sn-BTO12 (79.2 %), at microwave frequencies comparable tunabilities were achieved for Sn-BTO12 (39.2 %) and Sn-BTO14 (38.2 %). The difference in relative tunabilities between low and high frequencies is attributed to the difference in activities between larger ferroelectric domains and polar nanoclusters at these frequencies, with the former relatively inactive at high frequencies. This study demonstrates that low frequency tunability is not always a good indicator of the high frequency performance due to the lack of a domain contribution.

1. Introduction

Modern wireless communication systems require an increasing number of active components to enable switchable and steerable antenna arrays to track moving targets [1,2]. This requirement becomes even more significant when operational frequencies are increased, as directed antennas need to address problems associated with increasing propagation loss caused by shorter wavelengths [3]. At the moment, this is accomplished using parts like varactors, pin diodes, MEMS switches, and semiconductors [4].

Tunable bulk ceramics, where dielectric permittivity changes with applied DC electric field, have the potential to replace non-tunable conventional materials currently used in components such as antennas. Their use could enable antennas to self-reconfigure tuning characteristics, including resonant frequency, radiation pattern and polarisation in response to the changing dielectric permittivity.

Barium titanate ($BaTiO_3$, BT) is regarded as a displacive ferroelectric with a tetragonal perovskite (ABO_3) structure in space group *P4mm*. At room temperature, Ti^{4+} ions are displaced in the $< 001 >$ direction with respect to the centre of the octahedral B-sites, resulting in spontaneous polarisation. BT exhibits several polymorphs including rhombohedral, orthorhombic, tetragonal and cubic phases [5]. Progressive strontium substitution into BT leads to the stabilisation of the cubic phase. The composition $Ba_{0.6}Sr_{0.4}TiO_3$(BST64) has been particularly well studied, due to its high dielectric tunability in the nominally paraelectric phase [6]. This behaviour has been attributed to the existence of randomly oriented polar nanoclusters which rapidly respond to an applied electric field. However, the voltage necessary to induce such switching is relatively high, which has hindered practical applications. This voltage can be reduced by preparation of BST64 as thin films, but is accompanied by an increase in dielectric loss and reduced microwave performance [1]. Other compositions in the $Ba_{1-x}Sr_xTiO_3$ system also demonstrate substantial dielectric tunability, for example $Ba_{0.65}Sr_{0.35}TiO_3$ bulk ceramic shows a tunability of 68.6 % [7]. Additionally, BST64 based composites have been shown to exhibit reasonable tunabilities, such as $Ba_{0.6}Sr_{0.4}TiO_3/MgO$ [8] (with a tunability of 40 %), $Ba_{0.6}Sr_{0.4}TiO_3/Mg_2SiO_4/MgO$ [9] (with a tunability of 10.5 %) and Mn doped $Ba_{0.6}Sr_{0.4}TiO_3/MgO$ [10] (with a tunability of 27 %). Recently, a $Ba_{0.6}Sr_{0.4}TiO_3/PVDF$ (polyvinylidene fluoride) composite was shown to exhibit a high tunability of 78.3 % at a DC field of 190 kV mm^{-1} [11]. Notably, most of these tunability measurements were conducted at low frequencies ($<$ 100 MHz). At higher frequencies, such as in the microwave region, measurement of the dielectric tunability remains challenging due to the difficulty in measuring microwave permittivity and loss under a DC bias
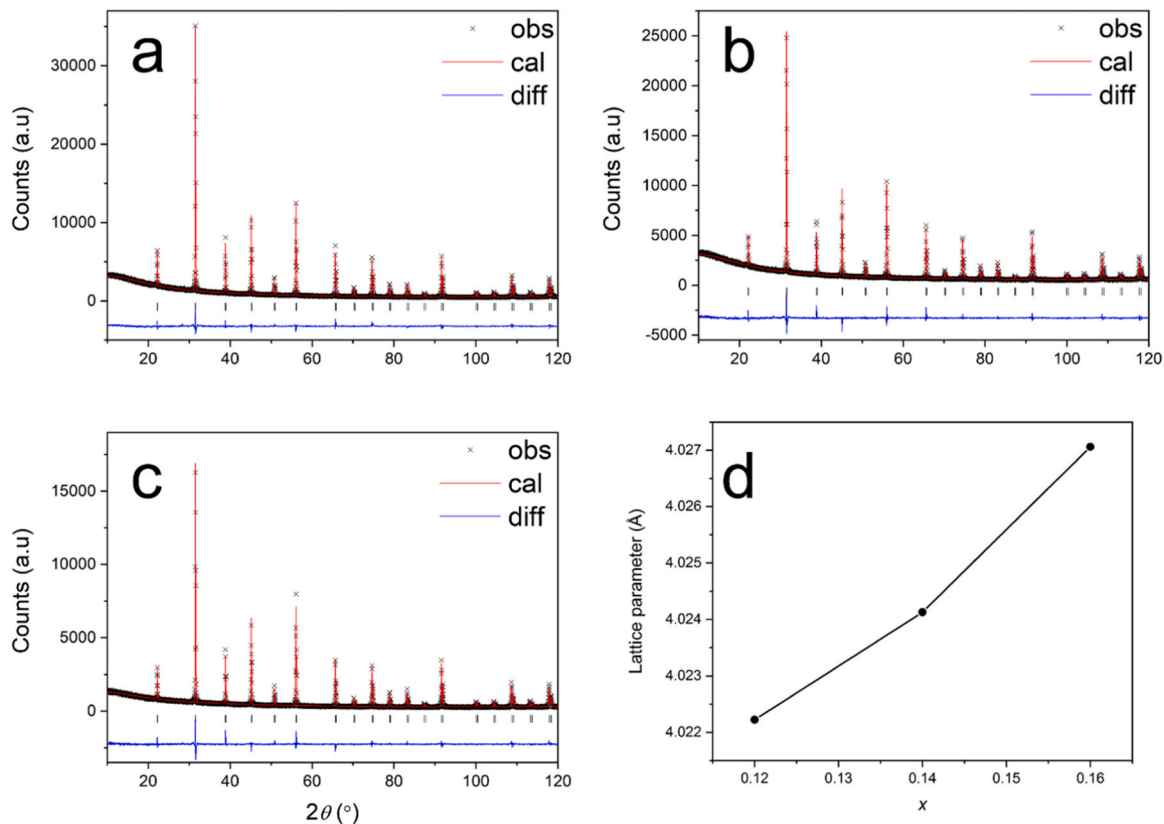

Fig. 1. Fitted XRD profiles for (a) Sn-BTO12, (b) Sn-BTO14 and (c) Sn-BTO16, and (d) compositional variation of cubic lattice parameter.

field. However, using a coplanar waveguide method, such measurements are possible, as demonstrated in the case of strontium titanate thin films of composition $Sr_7Ti_7O_{19}$, where a microwave dielectric tunability of 20 % was recorded [12]. Such measurements of dielectric properties at microwave frequencies can provide valuable insights for the design and simulation of microwave communication devices.

B-site substitution by tin in BT ($BaTi_{1-x}Sn_xO_3$, Sn-BTO) has been shown to lower the Curie point with increasing level of substitution and reaches values below room temperature at $x = 0.15$ [13,14]. Sn-BTO was found to transform from a normal ferroelectric to a relaxor ferroelectric with increasing x-value, accompanied by an increase in the diffuseness of the tetragonal to cubic phase transition for $x > 0.19$ [15–17]. Sn-BTO exhibits good tunability at low frequency, comparable to that of BST64 [18]. To date, the microwave tunability of Sn-BTO ceramics has not been reported.

In this work, a systematic study of Sn-BTO bulk ceramics has been carried out, including measurements of the dielectric and ferroelectric properties. Unusually for a ceramic material, we measure and compare the tunabilities at both low and high frequencies and correlate the behaviour with changes in local structure. Sn-BTO shows differences in tunability behaviour at low and high frequencies attributed to the coexistence of polar nanoclusters and polar regions, which show different activities in these frequency ranges.

2. Experimental

Barium tin titanate $BaTi_{(1-x)}Sn_xO_3$ (Sn-BTOx, $x = 0.12$, 0.14 and 0.16) ceramics were synthesised by solid state methods. Stoichiometric amounts of barium carbonate ($BaCO_3$, Aldrich, 99 %), titanium oxide (TiO_2, Aldrich, 99.8 %) and tin oxide (SnO_2, Aldrich, 99.9 %) were milled on a planetary ball mill (Fritsch Pulverisette 5/4 classic line, Germany) at 180 rpm for 24 h in a nylon jar, filled with zirconia balls, using ethanol as a dispersant. After drying and sieving, the collected

powder was calcined at 1000 °C for 4 h, and, after cooling, ball milled, dried and sieved again. The resulting powder was pelletized (150 MPa), to yield pellets of 13 mm diameter and approximately 1 mm thickness and sintered at 1350 °C for 2 h. Pellet densities were measured by the Archimedes method via the displacement of water.

X-ray powder diffraction (XRD) of the studied compositions was carried out on a PANalytical Cubix3 diffractometer, fitted with a PIXcel (1D) detector, using Ni filtered Cu-Kα radiation ($\lambda = 1.5418$ Å). Data were collected at room temperature in flat plate Bragg-Brentano geometry over the 2θ range of 5–120°, with a step width of 0.0315° and an effective count time of 200 s per step. Collected data were modelled by Rietveld analysis using the GSAS suite of programs [19]. Structure refinement was carried out in the cubic space group *Pm-3m* [20]. Scanning electron microscopy (SEM, FEI Inspect F) images were recorded on polished and fracture surfaces of the ceramic samples. Prior to measurement, the surfaces of the ceramic samples were polished with abrasive papers and thermally etched at 1100 °C for 20 min.

A Renishaw Via™ confocal Raman microscope was used to measure the Raman spectra of the ceramic samples with an argon laser (633 nm wavelength). X-ray photoelectron spectroscopy (XPS, ThermoFisher Nexsa Xray Photoelectron spectrometer) was used to characterise the surface speciation. The sample surface was polished using abrasive papers prior to the XPS characterisation.

For electrical characterisation, ceramic pellets were cut using a diamond saw to give plates of 4 mm × 4 mm × 0.3 mm, coated with silver paste (Gwent Electronic Materials Ltd. Pontypool, U.K.) and heated at 450 °C for 30 min to form conductive electrodes. The dielectric properties of the ceramics at low frequencies (up to 1 MHz) were measured using a precision impedance analyser (Agilent 4294 A). The temperature variation of dielectric properties was measured using an LCR meter (Agilent 4284 A) connected to a homemade temperature control chamber. Current-electric field (*I-E*), polarisation-electric field (*P-E*) and strain-electric field (*S-E*) loops were measured using a
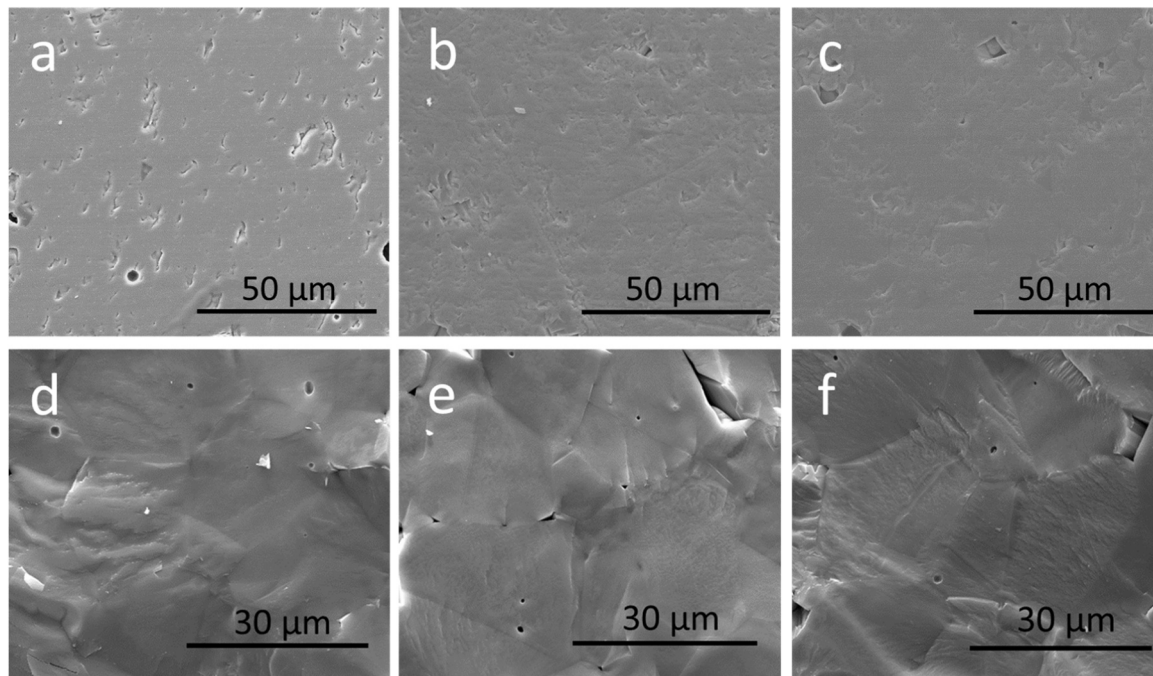
Fig. 2. SEM images of the (a-c) polished and (d-f) fracture surfaces for (a, d) Sn-BTO12, (b, e) Sn-BTO14 and (c, f) Sn-BTO16 ceramics.
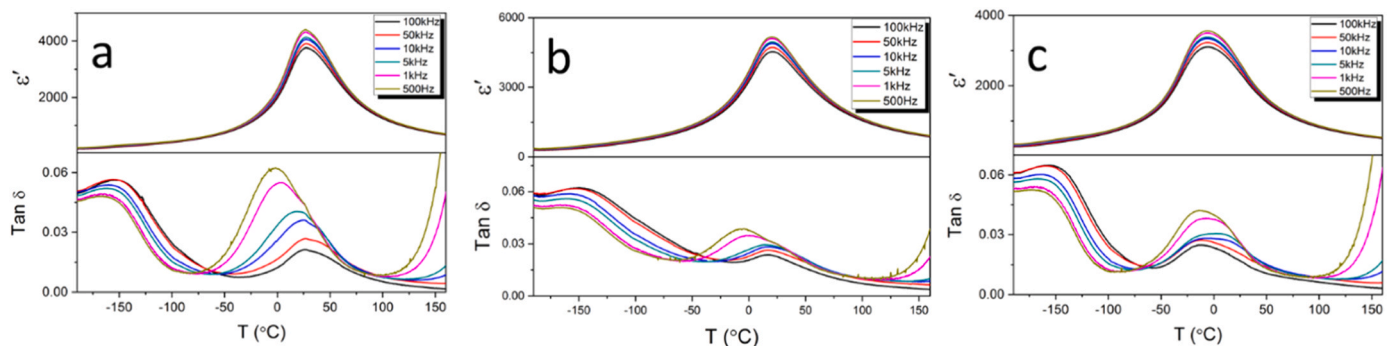

Fig. 3. Thermal variation of dielectric permittivity and loss for (a) Sn-BTO12, (b) Sn-BTO14 and (c) Sn-BTO16.

ferroelectric hysteresis tester (NPL, UK), with voltage applied in a triangle waveform.[21].

The dielectric tunability was measured by depositing a co-planar waveguide (CPW) transmission line onto the surface of the ceramic samples through a thermally evaporated gold coating. The tunability at microwave frequencies was retrieved from the propagation constant via measurements of the 2-port S-parameters using a PNA-L N5230C Vector Network Analyzer with a fully calibrated GSG microprobe 525. The length of the CPW transmission line was 5 mm, and the thickness of the gold coating was about 100 nm.

3. Results and discussion

XRD patterns of the studied compositions show a single phase perovskite structure with no detectable impurities (Fig. 1) and were well-fitted using a cubic model in space group *Pm-3m*. This is consistent with the system possessing an average non-polar structure, as previously reported for related BT based systems [14,15,17,22,23]. The details of the refinement parameters are summarised in Table S1. The lattice parameter of the unit cell increased with increasing tin concentration, consistent with the substitution of the smaller Ti^{4+} ions being replaced by larger Sn^{4+} ions ($r = 0.605$ Å and 0.690 Å in six coordinate geometry,

respectively) [24].

The relative pellet densities were found to be 95.5 %, 96.8 % and 95.1 % for Sn-BTO12, Sn-BTO14 and Sn-BTO16 ceramic samples, respectively. SEM images of the polished and fracture surface of the ceramics reveal densely packed grains with a few micron sized pores (Fig. 2). The grain size is relatively large, ca. 25 μm, for all the studied compositions. It is noteworthy, that all of the SEM images show transgranular fracture, indicating strong bonding between grains.

The temperature dependencies of dielectric permittivity and loss for the studied compositions are shown in Fig. 3. A single dielectric permittivity peak was observed for all compositions corresponding to the Curie point (T_c). With increasing level of substitution, the dielectric permittivity peak shifts to lower temperature, with T_c values of 28, 18 and -6 °C for the $x = 0.12$, 0.14 and 0.16 compositions, respectively. While the dielectric permittivity peak corresponding to T_c shows some frequency dependence (decreasing permittivity with increasing frequency), the permittivity spectra generally show minimal frequency dependence over the studied temperature range. Such frequency dependence of the maximum permittivity is typically associated with the presence of polar nanoclusters [15], which have a range of sizes with different activation energies for switching, and are more sensitive to frequency and temperature. At $x = 0.0$, BT is in the tetragonal
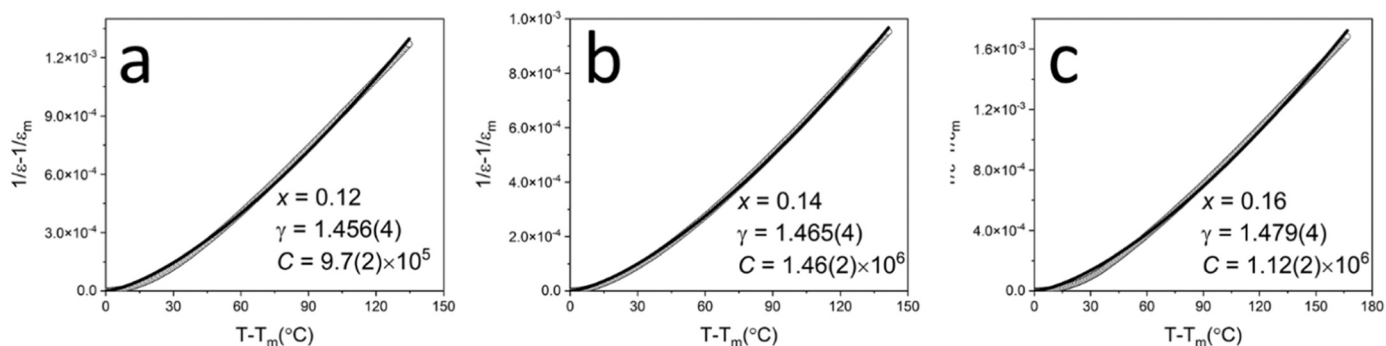
Fig. 4. Dielectric permittivity data at 100 kHz fitted by the modified Curie-Weiss law for (a) Sn-BTO12, (b) Sn-BTO14 and (c) Sn-BTO16.
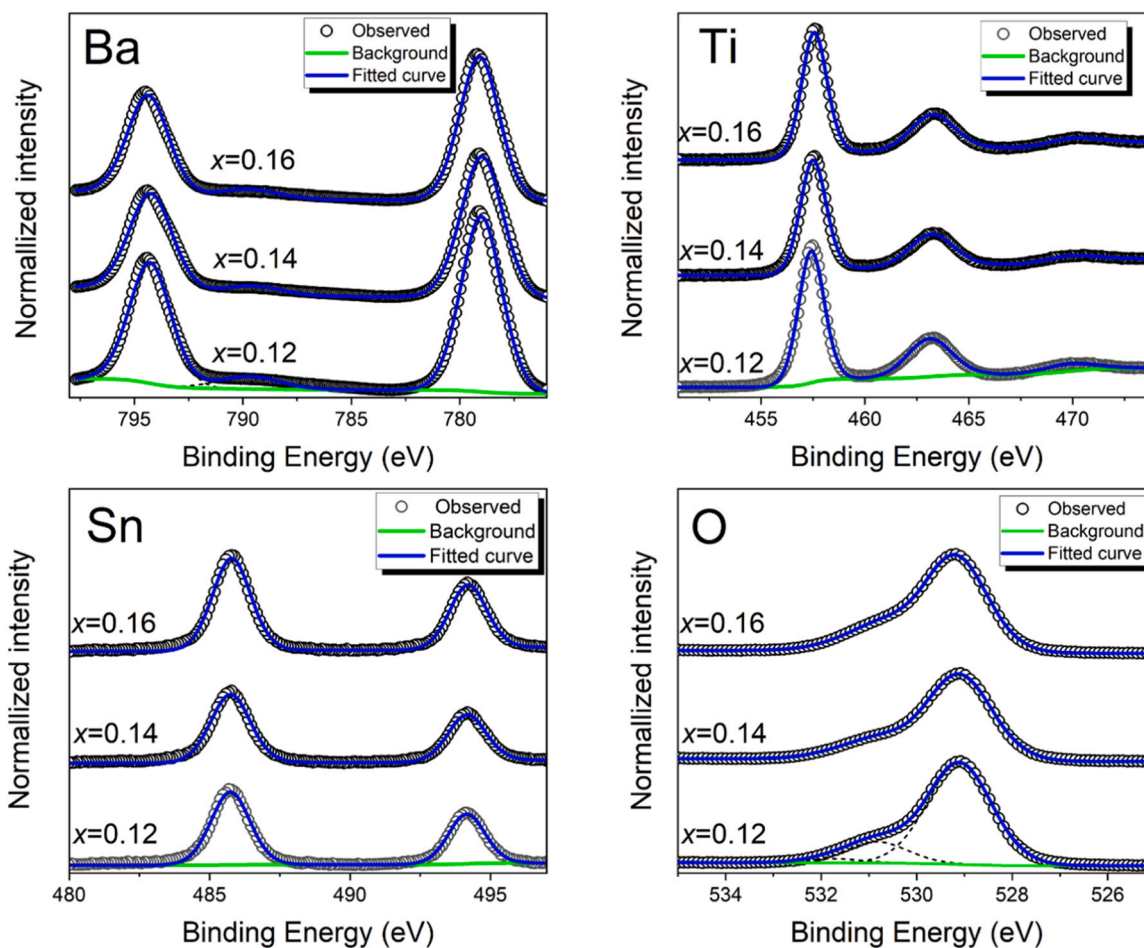

Fig. 5. Fitted XPS results for the studied SN-BTO*x* compositions.

ferroelectric state at room temperature with a T_c value of ca. 120 °C. Sn substitution into BT interrupts the long-range FE ordering and results in a lowering of the T_c value, to at or below room temperature, leaving the nominally paraelectric cubic phase evident in the XRD patterns (Fig. 1). Although the dielectric permittivity peaks show little frequency dependency over the measured frequency range, the dielectric loss peaks near the Curie point shift to higher temperatures at higher frequencies, and thus do exhibit frequency dependency, indicative of relaxor behaviour. At around − 150 °C, a second dielectric loss peak is observed, which also shows similar frequency dependency. However, no anomalies are observed in the dielectric permittivity plots at the corresponding temperatures. This suggests that the loss peaks correspond to a phase transition between two different FE phases [25].

To further investigate the suggested relaxor behaviour for the studied compositions, the permittivity above T_c measured at 100 kHz was analysed using the modified Curie Weiss Law (Fig. 4) and its temperature dependence fitted using Eq. 1.

$$\frac{1}{\varepsilon''} = \frac{1}{\varepsilon''_m} + \frac{(T - T_m)^\gamma}{C}$$
(1)

where T_m is the temperature of maximum permittivity, C is the Curie-Weiss constant and γ is a measure of the degree of diffuseness in dielectric properties; where normal ferroelectric and ideal relaxor ferroelectric materials have γ values of 1 and 2, respectively [25]. According to the fitted solid line, the γ value of the studied compositions
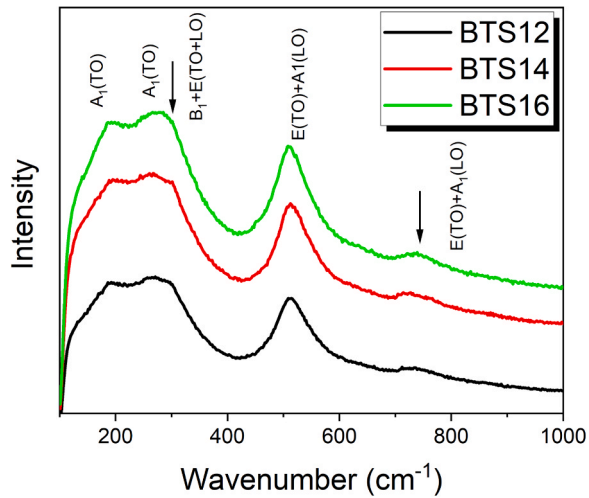
Fig. 6. Raman spectra for the studied Sn-BTO*x* compositions.

ranged from 1.45 to 1.48, with the value increasing with increasing Sn concentration, indicating that Sn substitution enhances diffuseness. The results confirm relaxor-like behaviour for the SN-BTO system. Bearing in mind the average non-polar structure seen in the XRD results (Fig. 1), it can be proposed that increasing substitution of Ti^{4+} by Sn^{4+} in BT causes disruption of the long-range FE ordering leading to increasingly smaller

FE regions, which, in the compositional range studied, are randomly distributed in an average non-polar matrix.

XPS was used to analyse the chemical environments of individual elements in the studied compositions (Fig. 5). The sample surface was ion etched for 3 min using an Ar cluster to reduce the surface contamination. All scanned spectra were calibrated using the C 1 s peak and peaks fitted using a Gaussian-Lorentzian function. The fitted parameters are summarized in Table S2. In general, there are no significant differences in the scanned elemental spectra for the studied compositions. The Ti 2p and Sn 3d binding energies increase with increasing Sn substitution. The binding energy is a measure of the attraction of the core electrons to the nucleus. On Sn substitution, the lattice shows chemical expansion (Fig. 1d) with a consequent lengthening of the B-O bond lengths, i.e., the valence electrons are drawn away from the nuclei, leading to a stronger attraction between the nucleus and the core electrons.

For Sn-BTO12, the oxygen spectrum was fitted to three peaks with binding energies of 529.1, 530.82 and 531.74 eV. Noting that the XPS method is a surface sensitive technique, these can be attributed to oxygen atoms in regular lattice sites, those close to oxygen vacancies and surface adsorbed oxygen, respectively [26–28]. The amount of adsorbed oxygen in the studied compositions was noticeably low due to the ion etching process. While the peak at 530.82 eV is not a direct measure of the oxygen vacancy concentration, it can be used to give a relative indication of trends in the vacancy concentration when compared to other compositions. Considering only the regular lattice and "vacancy" oxygen peaks, the proportions of "vacancy" oxygen are similar for the
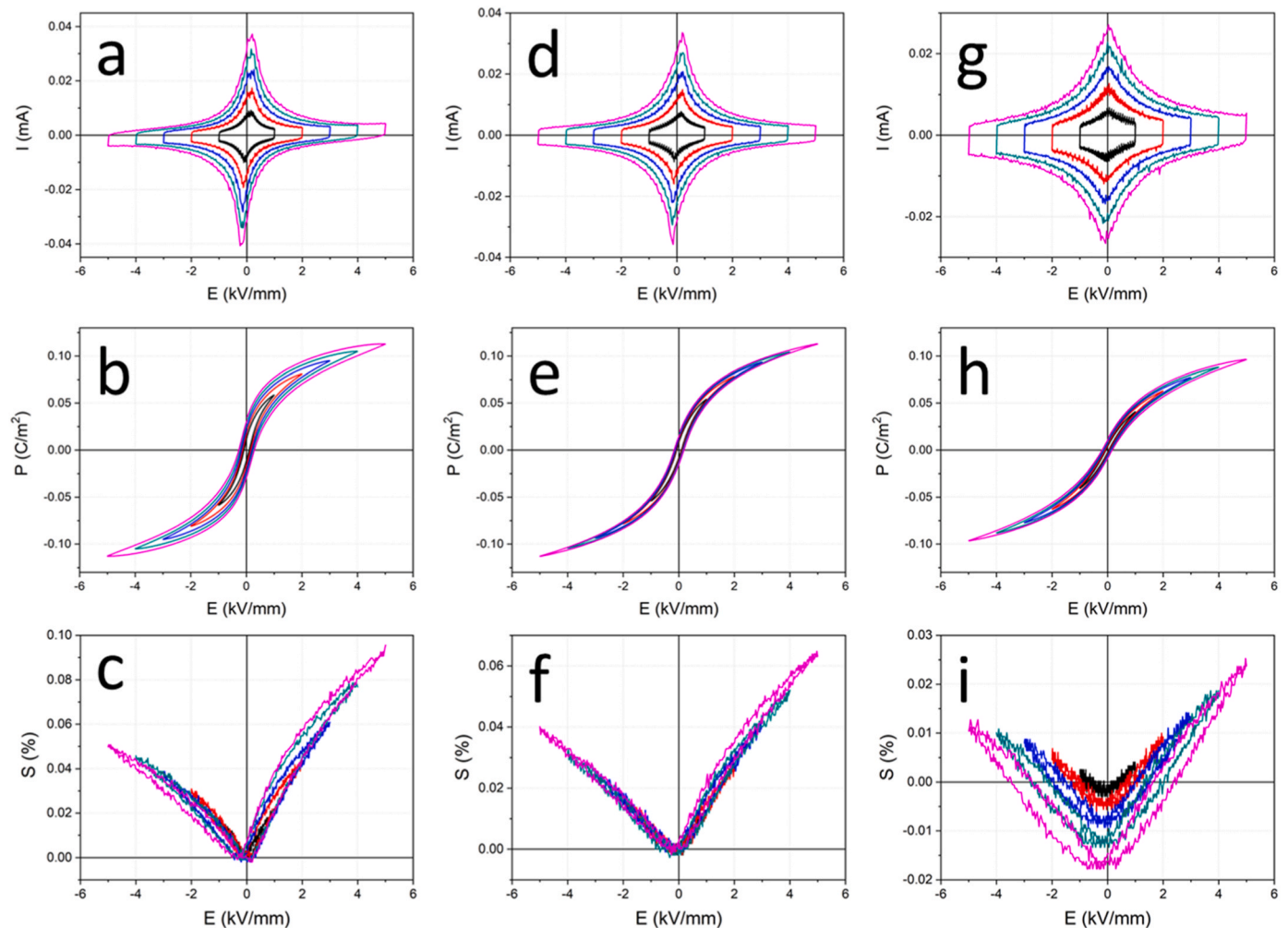

Fig. 7. (a, d, g) *I-E*, (b, e, h) *P-E* and (c, f, i) *S-E* loops measured at 1 Hz for (a-c) Sn-BTO12 (d-f) Sn-BTO14 and (g-i) Sn-BTO16 compositions.
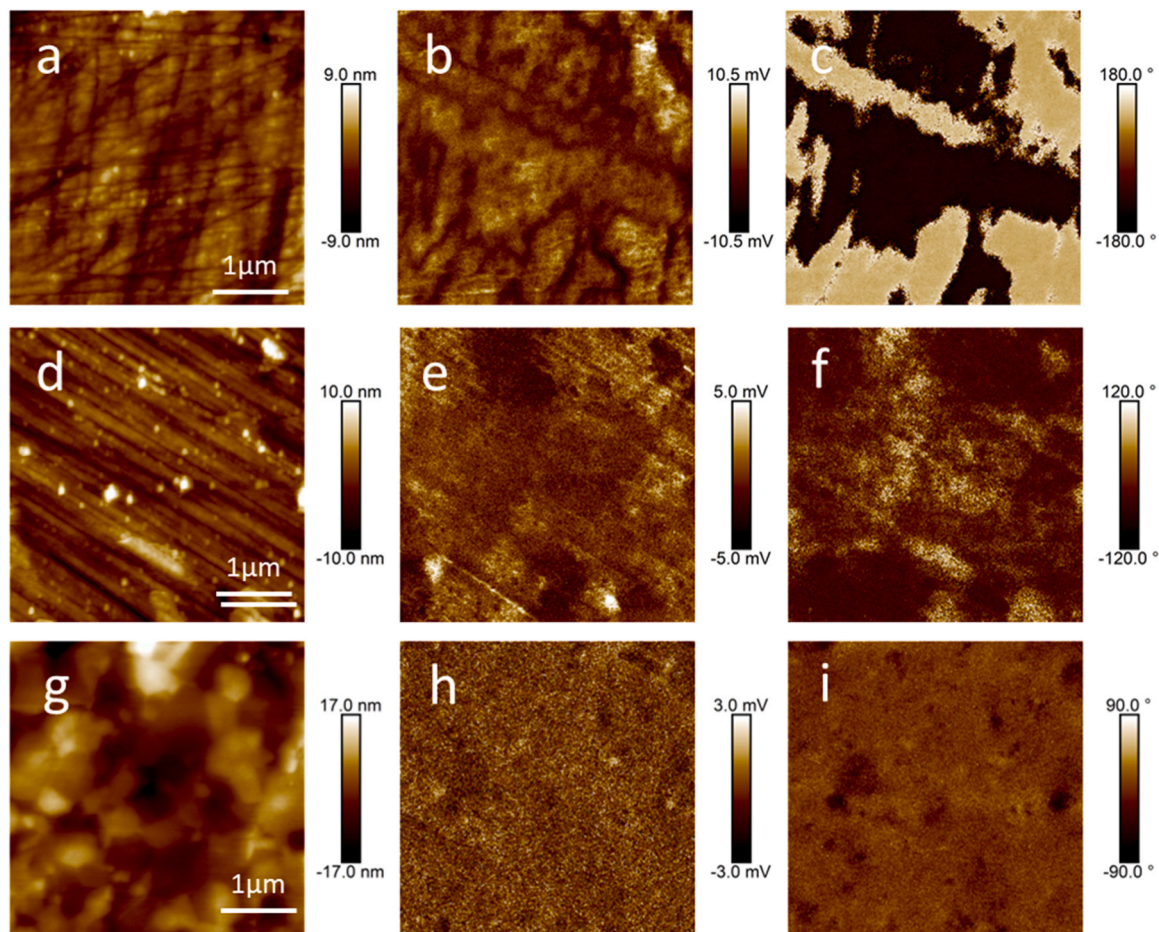
Fig. 8. PFM images for (a-c) Sn-BTO12, (d-f) Sn-BTO14 and (g-i) Sn-BTO16, including (a, d, g) height, (b, e, h) amplitude and (c, f, i) phase images.

two lowest *x*-value compositions at 16.5 % and 15.9 %, while that for Sn-BTO16 was significantly higher at 20.5 %, suggesting an increase in oxygen vacancy concentration for this composition. Due to the high sintering temperature used in the preparation of the ceramics, some degree of Ti reduction is unavoidable leading to the presence of low concentrations of oxygen vacancies which contribute to the dielectric loss.[29].

Raman spectroscopy was used to explore the local structure of the Sn-BTO compositions (Fig. 6). The allowed vibrational modes corresponding to the cubic perovskite structure were used to identify the majority of peaks [30–32]. The two additional peaks, marked by arrows in Fig. 6, were attributed to vibrational modes in the polar tetragonal structure and are forbidden in the non-polar cubic structure [6,30,31], despite the XRD analysis showing an average non-polar structure. This would be consistent with the presence of local polar regions in a non-polar matrix. Additionally, for Sn-BTO compositions with low levels of Sn substitution, the 300 cm^{-1} wavenumber peak was more pronounced, which may be related to an increase in the size and or concentration of these polar regions in the materials.

Room temperature *I-E*, *P-E* and *S-E* loops for the studied compositions at 1 Hz with an electric field up to 5 kV mm^{-1} are shown in Fig. 7. For Sn-BTO compositions with higher Sn substitution, the current peaks gradually broadened as peak positions shifted to lower electric fields. In general, the current peak profile in *I-E* loops indicates the tunability performance, where materials having better tunability exhibit sharper current peaks. Additionally, the presence of current peaks near zero electric field is attributed to the presence of polar nanoclusters, which can be aligned and recovered by applying and removing the electric field, respectively. For high *x*-value compositions in the Sn-BTO system,

P-E hysteresis loops were narrower with lower saturation polarisation and remanent polarisation, which indicates lower loss under high electric field. High electric fields caused the Sn-BTO12 sample to exhibit a notable current tilting, which is indicative of leakage current in the material and results in large *P-E* hysteresis loops. The large remanent polarisation in Sn-BTO12 indicates the existence of ferroelectric domains in the material. Although the saturation polarisation value was similar for Sn-BTO12 (0.1129 C cm^{-2}) and Sn-BTO14 (0.1128 C cm^{-2}) and larger than that of Sn-BTO16 (0.0962 C cm^{-2}) compositions, the electric field induced strain was significantly higher for Sn-BTO12 (0.09 %) compared to those of Sn-BTO14 (0.06 %) and Sn-BTO16 (0.04 %). The higher strain obtained in Sn-BTO12 might be attributed to the existence of larger polar regions or domains.

PFM was carried out on the polished surface of the ceramics, in order to analyse the local polar structure in the materials (Fig. 8). For Sn-BTO12 and Sn-BTO14 samples, the roughness of the scanned areas was less than 20 nm, with some minor scratching from the polishing procedure. A roughness value of around 34 nm was seen for the Sn-BTO16 sample. The surface morphology was noticeably different from the amplitude and phase images, indicating that the surface roughness had little impact on the piezoelectric response. When compared to Sn-BTO14, the difference in phase contrast for Sn-BTO12 was more pronounced. Both nanoscale and microscale polar regions were evident in Sn-BTO12, corresponding to polar nanoclusters and ferroelectric domains, respectively. The co-existence of larger domains and polar nanoclusters in Sn-BTO12 is attributed to the large strain which is evident in the *S-E* loop (Fig. 8). The shape of the polar area shown in the phase image is clearly depicted in the amplitude image. However, due to the poor contrast in the amplitude and phase images of Sn-BTO14 and
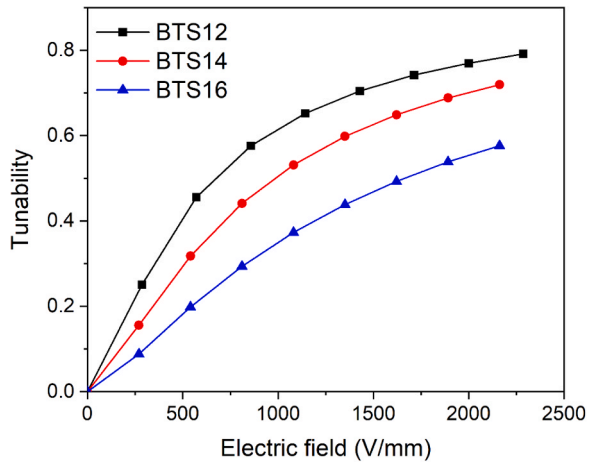
Fig. 9. Dielectric tunability of Sn-BTO*x* compositions measured at 100 kHz.

$$\eta = \frac{\varepsilon_0 - \varepsilon_E}{\varepsilon_0} \qquad (2)$$

where ε_E and ε_0 are the dielectric permittivity under a biased electric field and at zero field, respectively. The dielectric tunability of the studied compositions at 100 kHz increased dramatically at low electric field, reaching saturation at high electric field (Fig. 9). The Sn-BTO compositions with lower levels of Sn substitution exhibit higher dielectric tunability. A maximum dielectric tunability of 79.2 % was achieved for the Sn-BTO12 composition under an electric field of 2.3 kV mm^{-1}. The low frequency tunability demonstrated by this material is significantly higher than most reported materials and comparable to that seen in the Ba$_{0.6}$Sr$_{0.4}$TiO$_3$/PVDF(polyvinylidene fluoride) composite [11], but in the present case this tunability was achieved at a much lower voltage. When a DC electric field is applied, the polar clusters align and their activity is restrained, which reduces their contribution to the dielectric permittivity. At high electric field, the tunability of the studied compositions slowly increases as they approach saturation polarisation. The high tunability of Sn-BTO12 is attributed here to the presence of both polar nanoclusters and larger ferroelectric domains in the materials.

Fig. 10 shows the dielectric tunabilities of the Sn-BTO compositions at microwave frequencies. The DC electric field was applied to a transmission line, coated on the sample surface. As expected, the dielectric permittivity decreased with increasing frequency. The microwave tunability of all Sn-BTO compositions increased with increasing applied voltage, which is consistent with the low frequency tunability results. This can be explained by considering that at microwave frequencies, the

Sn-BTO16, the polar areas are difficult to distinguish. The degree of polarisation decreases with increasing level of Sn substitution, resulting in a weaker piezoelectric response. As a result, the phase image of the Sn-BTO12 sample shows a clear polar domain as well as small polar clusters, while those for Sn-BTO14 and Sn-BTO16 exhibit fewer pronounced polar clusters.

The dielectric tunability (η) of the studied compositions was calculated from the changes in permittivity using Eq. (2).
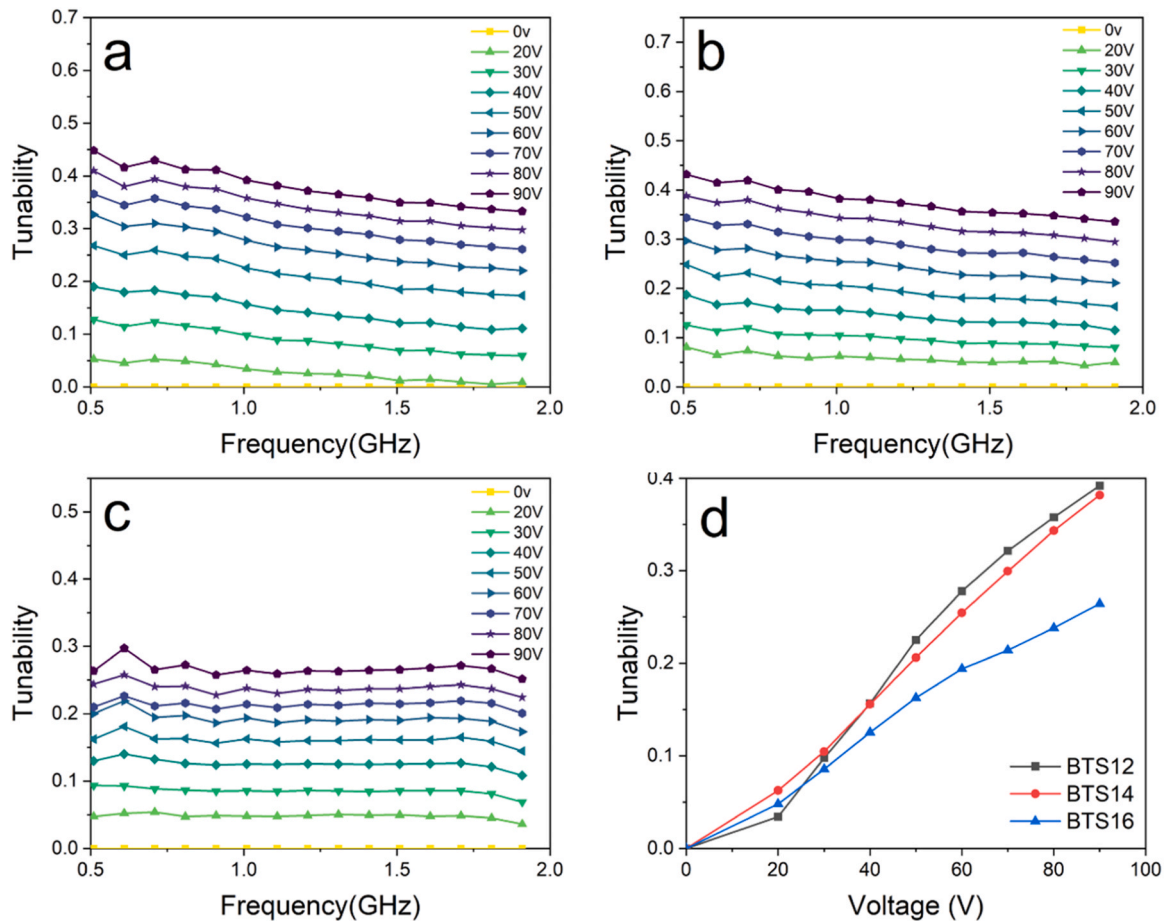

Fig. 10. Dielectric tunabilities of (a) Sn-BTO12, (b) Sn-BTO14 and (c) Sn-BTO 16 measured at microwave frequencies and (d) the tunability changes with voltage at 1 GHz.

polar nanoclusters remained active and the influence of the DC field on them was still significant. In contrast to the situation at lower frequencies, at microwave frequencies saturation polarisation was not approached due to the limited maximum voltage (90 V) possible in the experiment. The highest tunability of 39.2 % was achieved for the Sn-BTO12 sample at 1 GHz. Although the tunability of Sn-BTO12 is significantly higher at low frequencies compared to those for Sn-BTO14 and Sn-BTO16, the tunability at microwave frequencies was similar for Sn-BTO12 and Sn-BTO14 but still significantly higher than that for Sn-BTO16. For the Sn-BTO12 composition, the high tunability at low frequencies is attributed to the co-existence of larger ferroelectric domains and smaller polar nanoclusters. However, domains, by definition, are large in size and their polarisation response is slow, which results in a lack of activity at microwave frequencies. Therefore, at microwave frequencies, the main contribution to the tunability is from the polar nanoclusters and leads to comparable tunability values for Sn-BTO12 and Sn-BTO14, while for Sn-BTO16, the low concentration of polar nanoclusters results in low tunability at these frequencies.

4. Conclusions

Tin substituted barium titanate compositions were successfully synthesised by conventional solid state methods. Although XRD analysis on Sn-BTO powders shows an average cubic structure, Raman spectroscopy, *P-E* and *I-E* behaviour and PFM analysis reveal the presence of local polar regions in the material, which are responsible for high tunability under DC electric fields. The chemical environments of the constituent elements in the studied compositions were examined by XPS, and revealed that tin substitution in the Sn-BTO system increases the binding energy of the perovskite B-site ions, which might be caused by strain induced changes in the oxygen sublattice. *P-E* and *I-E* loops for Sn-BTO14 and Sn-BTO16 compositions show narrow non-linear hysteresis loops with sharp current peaks indicating high tunability and low loss under electric field, while for Sn-BTO12 the large area of the *P-E* loops indicates high loss. *S-E* loops and PFM analysis indicate the presence of domains and polar nanoclusters in Sn-BTO12 and only polar nanoclusters in Sn-BTO14 and Sn-BTO16.

Sn-BTO12 shows the highest tunability of 79.2 % at low frequencies, significantly higher than seen in Sn-BTO14 and Sn-BTO16. However, at microwave frequencies, Sn-BTO12 and SnBTO14 have similar maximum tunabilities of around 39 % at 1 GHz, significantly higher than that of Sn-BTO16. The different tunabilities of the examined compositions at low and high frequencies clearly demonstrate that while domains contribute to the tunability at low frequencies, they are inactive at high frequencies. Polar nanoclusters continue to be active at both low and high frequencies and contribute to the tunability. This conclusion is important for the design of tunable materials since, as this work shows, the tunability at low frequencies is not always a good indicator of the tunability at higher frequencies.

Declaration of Competing Interest

The authors declare that they have no known competing financial interests or personal relationships that could have appeared to influence the work reported in this paper.

Data availability

Data will be made available on request.

Acknowledgements

Appendix A. Supporting information

Supplementary data associated with this article can be found in the online version at doi:10.1016/j.jeurceramsoc.2023.10.033.

References

[1] A.K. Tagantsev, V.O. Sherman, K.F. Astafiev, J. Venkatesh, N. Setter, Ferroelectric materials for microwave tunable applications, J. Electroceram. 11 (2003) 5–66, https://doi.org/10.1023/B:JECR.0000015661.81386.e6.

[2] J.P. Turpin, J.A. Bossard, K.L. Morgan, D.H. Werner, P.L. Werner, Reconfigurable and tunable metamaterials: a review of the theory and applications, Int. J. Antennas Propag. 2014 (2014) 1–18, https://doi.org/10.1155/2014/429837.

[3] R.L. Haupt, M. Lanagan, Reconfigurable antennas, IEEE Antennas Propag. Mag. 55 (2013) 49–61, https://doi.org/10.1109/MAP.2013.6474484.

[4] J. Costantine, Y. Tawk, S.E. Barbin, C.G. Christodoulou, Reconfigurable antennas: design and applications, Proc. IEEE 103 (2015) 424–437, https://doi.org/10.1109/JPROC.2015.2396000.

[5] M. Acosta, N. Novak, V. Rojas, S. Patel, R. Vaish, J. Koruza, G.A. Rossetti, J. Rödel, BaTiO3-based piezoelectrics: fundamentals, current status, and perspectives, Appl. Phys. Rev. 4 (2017), https://doi.org/10.1063/1.4990046.

[6] H. Zhang, H. Giddens, Y. Yue, X. Xu, V. Araullo-Peters, V. Koval, M. Palma, I. Abrahams, H. Yan, Y. Hao, Polar nano-clusters in nominally paraelectric ceramics demonstrating high microwave tunability for wireless communication, J. Eur. Ceram. Soc. 40 (2020) 3996–4003, https://doi.org/10.1016/j.jeurceramsoc.2020.04.015.

[7] P.Z. Ge, X.G. Tang, Q.X. Liu, Y.P. Jiang, W.H. Li, B. Li, Temperature-dependent dielectric relaxation and high tunability of (Ba1-xSrx)TiO3ceramics, J. Alloy. Compd. 731 (2018) 70–77, https://doi.org/10.1016/j.jallcom.2017.09.330.

[8] U.C. Chung, C. Elissalde, M. Maglione, C. Estournès, M. Paté, J.P. Ganne, Low-losses, highly tunable Ba0.6 Sr0.4 Ti O3 MgO composite, Appl. Phys. Lett. 92 (2008) 0–3, https://doi.org/10.1063/1.2837621.

[9] Y. He, Y. Xu, T. Liu, C. Zeng, W. Chen, Microstructure and dielectric tunable properties of Ba0.6Sr 0.4TiO3-Mg2SiO4-MgO composite, IEEE Trans. Ultrason. Ferroelectr. Freq. Control. 57 (2010) 1505–1512, https://doi.org/10.1109/TUFFC.2010.1581.

[10] J. Cui, G. Dong, Z. Yang, J. Du, Low dielectric loss and enhanced tunable properties of Mn-doped BST/MgO composites, J. Alloy. Compd. 490 (2010) 353–357, https://doi.org/10.1016/j.jallcom.2009.09.185.

[11] Y. Guo, S. Liu, S. Wu, J. Xu, E. Pawlikowska, W. Bulejak, M. Szafran, A. Rydosz, F. Gao, Enhanced tunable dielectric properties of Ba0.6Sr0.4TiO3/PVDF composites through dual-gradient structural engineering, J. Alloy. Compd. 920 (2022), https://doi.org/10.1016/j.jallcom.2022.166034.

[12] C.H. Lee, N.D. Orloff, T. Birol, Y. Zhu, V. Goian, E. Rocas, R. Haislmaier, E. Vlahos, J.A. Mundy, L.F. Kourkoutis, Y. Nie, M.D. Biegalski, J. Zhang, M. Bernhagen, N. A. Benedek, Y. Kim, J.D. Brock, R. Uecker, X.X. Xi, V. Gopalan, D. Nuzhnyy, S. Kamba, D.A. Muller, I. Takeuchi, J.C. Booth, C.J. Fennie, D.G. Schlom, Exploiting dimensionality and defect mitigation to create tunable microwave dielectrics, Nature 502 (2013) 532–536, https://doi.org/10.1038/nature12582.

[13] P. Ren, Z. Liu, Q. Wang, B. Peng, S. Ke, H. Fan, G. Zhao, Large nonlinear dielectric behavior in BaTi1−xSnxO3, Sci. Rep. 7 (2017) 6693, https://doi.org/10.1038/s41598-017-07192-x.

[14] W. Xiaoyong, F. Yujun, Y. Xi, Dielectric relaxation behavior in barium stannate titanate ferroelectric ceramics with diffused phase transition, Appl. Phys. Lett. 83 (2003) 2031–2033, https://doi.org/10.1063/1.1609037.

[15] C. Lei, A.A. Bokov, Z.G. Ye, Ferroelectric to relaxor crossover and dielectric phase diagram in the BaTi O3 -BaSn O3 system, J. Appl. Phys. 101 (2007), https://doi.org/10.1063/1.2715522.

[16] V.V. Shvartsman, W. Kleemann, J. Dec, Z.K. Xu, S.G. Lu, Diffuse phase transition in BaTi1-xSnxO3 ceramics: an intermediate state between ferroelectric and relaxor behavior, J. Appl. Phys. 99 (2006), https://doi.org/10.1063/1.2207828.

[17] W. Kleemann, S. Miga, Z.K. Xu, S.G. Lu, J. Dec, Non-linear permittivity study of the crossover from ferroelectric to relaxor and cluster glass in BaTi1−xSnxO3 (x = 0.175–0.30), Appl. Phys. Lett. 104 (2014) 0–4, https://doi.org/10.1063/1.4875595.

[18] S.G. Lu, Z.K. Xu, H. Chen, Tunability and reiaxor properties of ferroelectric barium stannate titanate ceramics, Appl. Phys. Lett. 85 (2004) 5319–5321, https://doi.org/10.1063/1.1829794.

[19] R.B. Von Dreele, A.C. Larson. Los Alamos National Laboratory Report, No, LAUR-8, 1987.

[20] H. Zhang, B. Yang, A.D. Fortes, H. Yan, I. Abrahams, Structure and dielectric properties of double A-site doped bismuth sodium titanate relaxor ferroelectrics for high power energy storage applications, J. Mater. Chem. A. 8 (2020) 23965–23973, https://doi.org/10.1039/d0ta07772k.

[21] J. Wu, A. Mahajan, L. Riekehr, H. Zhang, B. Yang, N. Meng, Z. Zhang, H. Yan, Perovskite Srx(Bi1−xNa0.97−xLi0.03)0.5TiO3 ceramics with polar nano regions for high power energy storage, Nano Energy 50 (2018) 723–732, https://doi.org/10.1016/j.nanoen.2018.06.016.

[22] X. Wei, Y. Feng, X. Yao, Slow relaxation of field-induced piezoelectric resonance in paraelectric barium stannate titanate, Appl. Phys. Lett. 84 (2004) 1534–1536, https://doi.org/10.1063/1.1655694.

[23] T. Wang, X.M. Chen, X.H. Zheng, Dielectric characteristics and tunability of barium stannate titanate ceramics, J. Electroceram. 11 (2003) 173–178, https://doi.org/10.1023/B:JECR.0000026372.07871.a4.

[24] R.D. Shannon, Revised effective ionic radii and systematic studies of interatomic distances in halides and chalcogenides, Acta Crystallogr. Sect. A 32 (1976) 751–767, https://doi.org/10.1107/S0567739476001551.

[25] K. Uchino, S. Nomura, Critical exponents of the dielectric constants in diffused-phase-transition crystals, Ferroelectrics 44 (1982) 55–61, https://doi.org/10.1080/00150198208260644.

[26] H.W. Cho, P. Pujar, M. Choi, S. Kang, S. Hong, J. Park, S. Baek, Y. Kim, J. Lee, S. Kim, Direct growth of orthorhombic Hf0.5Zr0.5O2 thin films for hysteresis-free MoS2 negative capacitance field-effect transistors, Npj 2D Mater. Appl. 5 (2021), 46, https://doi.org/10.1038/s41699-021-00229-w.

[27] Y. Goh, S.H. Cho, S.H.K. Park, S. Jeon, Oxygen vacancy control as a strategy to achieve highly reliable hafnia ferroelectrics using oxide electrode, Nanoscale 12 (2020) 9024–9031, https://doi.org/10.1039/d0nr00933d.

[28] C. Yu, Y. Zeng, B. Yang, R. Donnan, J. Huang, Z. Xiong, A. Mahajan, B. Shi, H. Ye, R. Binions, N.V. Tarakina, M.J. Reece, H. Yan, Titanium dioxide engineered for near-dispersionless high terahertz permittivity and ultra-low-loss, Sci. Rep. 7 (2017), 6639, https://doi.org/10.1038/s41598-017-07019-9.

[29] M. Pešić, F.P.G. Fengler, L. Larcher, A. Padovani, T. Schenk, E.D. Grimley, X. Sang, J.M. LeBeau, S. Slesazeck, U. Schroeder, T. Mikolajick, Physical mechanisms behind the field-cycling behavior of HfO2-based ferroelectric capacitors, Adv. Funct. Mater. 26 (2016) 4601–4612, https://doi.org/10.1002/adfm.201600590.

[30] M. El Marssi, F. Le Marrec, I.A. Lukyanchuk, M.G. Karkut, Ferroelectric transition in an epitaxial barium titanate thin film: Raman spectroscopy and X-ray diffraction study, J. Appl. Phys. 94 (2003) 3307–3312, https://doi.org/10.1063/1.1596720.

[31] M.B. Smith, K. Page, T. Siegrist, P.L. Redmond, E.C. Walter, R. Seshadri, L.E. Brus, M.L. Steigerwald, Crystal structure and the paraelectric-to-ferroelectric phase transition of nanoscale BaTiO3, J. Am. Chem. Soc. 130 (2008) 6955–6963, https://doi.org/10.1021/ja0758436.

[32] R.S. Katiyar, M. Jain, Y.I. Yuzyuk, Raman spectroscopy of bulk and thin-layer (Ba, Sr)TiO3 ferroelectrics, Ferroelectrics 303 (2004) 101–105, https://doi.org/10.1080/00150190490452857.